Accepted Manuscript
Version of record at: https://doi.org/10.1002/adom.202201193

Graphene Absorption Enhanced by Quasi-Bound-State-in-Continuum in Long-Wavelength Plasmonic-Photonic System

Thomas Kananen[1], Marcie Wiggins[2], Zi Wang[1], Feifan Wang[1], Anishkumar Soman[1], Karl Booksh[2], Andrea Alù[3], Tingyi Gu[1*]

[1] Department of Electrical and Computer Engineering, University of Delaware, Newark, DE 19711, United States

[2] Department of Chemistry and Biochemistry, University of Delaware, Newark, DE, 19716, United States

[3] Photonics Initiative, Advanced Science Research Center, City University of New York, New York, New York 10031, United States

* Email: tingyigu@udel.edu

Abstract:

Graphene plasmonic structures can support enhanced and localized light-mater interactions within extremely small mode volumes. However, the external quantum efficiency of the resulting devices is fundamentally limited by material scattering and radiation loss. Here we suppress such radiation loss channels by tailoring the structure to support a symmetry-protected bound-state-in-the-continuum (BIC) system. With practical loss rates and doping level in graphene, over 90% absorption near critical coupling is expected from numerical simulation. Experimentally measured peak absorption of 68% is achieved in such a tailored graphene photonic-plasmonic system, with maximum 50% contrast to the control sample without graphene. Significant reduction of the plasmon absorption for a different spacer thickness verifies the sensitivity of the system to the quasi-BIC condition.

Accepted Manuscript
Version of record at: https://doi.org/10.1002/adom.202201193

1. Introduction

Graphene plasmon polaritons are the hybrids of Dirac quasiparticles and infrared photons, enabling strong light-matter interactions within tightly confined mode [1-4]. The local field enhancement empowers graphene-based switches [5-10], photodetectors [11], molecular sensors [11-17] and photocatalytic response [18-19]. The intrinsic quantum efficiencies of those graphene plasmonic devices are limited by the mismatched plasmonic dissipation rate and its coupling rate to the incident photonic mode [19-21]. The large plasmon dissipation rate is attributed to hot carrier scattering, dielectric losses to the substrate's phonons and scattering from edge states or grain boundaries [1, 22]. To suppress the plasmonic dissipation channels, direct etching [23-25] and atop metal grating [12, 14-15] are replaced by the patterned semiconductor substrates [26], and the silicon oxide substrate is replaced by pristine boron nitride to eliminate electron-phonon coupling [27-29]. However, the monolayer graphene plasmon contribution to total absorption remains weak (<10%) [3, 15, 23, 28, 30-31]. On contrast, near unity absorption by the graphene layer can be achieved near critical coupling within photonic super-modes [32-35].

Without fine tuning, coupling the guided plasmonic mode to an out-of-plane photonic resonance mode can improve graphene absorption to 25% [24]. At a bound-state-in-the-continuum (BIC), the eigen state of a photonic-plasmonic hybrid mode can be decoupled from the radiative continuum, since the radiative quality factor is not simply constrained by the plasmonic mode scattering loss channels [36-39]. As the radiative quality factor of the local photonic-plasmonic mode rapidly deviates from the BIC condition, a balance between the radiation loss rate and the plasmonic loss rate can be reached, enabling critical coupling. A

Accepted Manuscript
Version of record at: https://doi.org/10.1002/adom.202201193

BIC-improved external quantum efficiency reduces the lasing threshold for both photonic and plasmonic modes [40-41], and the power threshold for harmonic generation in two-dimensional materials [42]. Plasmonic BICs have been theoretically explored in graphene [43-44] and silver gratings [45], and experimentally demonstrated with large quality factors (~145) in asymmetric gold plasmonic metasurface [46].

In this work, a graphene plasmon mode is defined by a micrometer-sized metal antenna array on a flat transparent zinc selenide (ZnSe) substrate. The spacing between the graphene plasmonic layer and the backside metal reflector determines the coupling between the in-plane guided plasmonic mode and the out-of-plane photonic cavity mode, and thus determines the features of the hybrid mode. To quantitatively evaluate the contribution of graphene, comparison of identical designs with and without graphene can provide direct evidence. More than 50% contrast in absorption spectra is observed experimentally in identical designs with and without graphene, compared to numerical simulations resulting in 80% extinction ratio contrast (excluding parasitic scattering loss). The additional layer of graphene leads to 10^3 field enhancement in the plasmonic mode. The results provide direct evidence of BIC-mediated plasmonic devices for efficient light interaction in single layer graphene. The BIC-enabled photon-plasmon efficient coupling can be utilized for nonlinear optics, harmonic generation, and optoelectronics in graphene plasmons.

2. Device fabrication and characterization

A uniform 100 nm gold layer is firstly deposited onto a silicon substrate through electron beam (e-beam) evaporation, serving as a backside reflector. The spacer layer of ZnSe is then thermally evaporated from a tantalum box with a perforated cover, with evaporation rate of 15

Accepted Manuscript
Version of record at: https://doi.org/10.1002/adom.202201193

angstrom per second. A bilayer ebeam resist is spin coated on the ZnSe on gold substrate to improve the edge sharpness of the gold plasmonic structure. After development, 50 nm gold is deposited onto the resist patterned substrate with a 10 nm chromium adhesive layer. The evaporation rate was kept at 5.05 Å/s for both layers. The chip is then placed in an NMP bath for metal liftoff. Large-scale graphene grown through chemical vapor deposition (CVD) is then transferred over the clean subwavelength metal arrays. The single layer nature of the graphene is verified by the combination of atomic force microscope and micro-Raman spectroscopy. A Bruker Optic Vertex 70 FTIR spectrometer and a Hyperion 2000 microscope with a single-point ATR crystal are used to characterize the reflectance spectra of the device, using a beam spot size of 40 μm. The reflection spectra are collected using OPUS 6.0 software averaging 128 scans per sweep. The reference background spectra are collected from the ZnSe/gold/silicon thin film and subtracted from the measured spectra.

3. Results analysis

The device schematics is shown in Fig. 1(a). The plasmonic mode is defined by the top planar gold nanorod array. ZnSe serves as the spacer material between the plasmon layer and backside reflector. The nanorod length (L), width (W), longitudinal periodicity (Λ), control the plasmonic modes. The optical spacer thickness (D) controls the coupling between the out-of-plane optical cavity mode and the in-plane plasmonic mode in the BIC system, yielding the BIC condition. The spacer material (ZnSe) is transparent in the long wavelength range, ensuring high quality factor optical cavity modes. Typical oxide dielectric materials are avoided due to their absorption at the designed spectral range. After transferring a monolayer graphene, distinguishable absorption spectra are shown in Fig. 1b. The addition of graphene

Accepted Manuscript
Version of record at: https://doi.org/10.1002/adom.202201193

shifts the absorption peak towards shorter wavelengths and enhances the peak absorption. Maximum contrast near 90% and 60% are observed in numerical simulation and experiment, respectively (Fig. 3). The inset of Fig. 1b shows the atomic force microscope image of the graphene on gold plasmonic nanostructure, with ZnSe spacer. The optical simulation of the three-dimensional structure shows strong optical field confinement in the graphene layer (Fig. 1c-d). The graphene layer manifests the in-plane optical field intensity, with over one order of magnitude enhancement (solid curve in Fig. 1e), compared to the same design without graphene (dashed curves in Fig. 1e). Without the back-side metal reflector, the weak reflection on ZnSe and silicon substrate result in one order of magnitude smaller field confinement in the top plasmonic layer (blue curves in Fig. 1e). Through the emergence of a BIC and associated tuning to critically coupling in its proximity, the optical field enhancement in the top graphene layer is more than 10^3. The detailed plasmonic mode profile is plotted in Fig. 1c. The Fermi-level dependent inter- and intra-band conductivity are considered in the 3D finite difference in time domain (FDTD) simulation (Supplementary Material SM I).

The reflection spectra of the hybrid plasmonic-photonic structure can be obtained from a Fabry-Perot-type approach [47]:

$$r_{total} = r + \frac{t^2 \exp(i2k_z D)}{1 - r\exp(i2k_z D)} \quad (1)$$

where k_z is the wave vector component perpendicular to the plasmon surface. k_z is the z component effective wavevector in ZnSe. r and t are the transmission and reflection coefficients for the surface plasmon, respectively. Both complex transmission and reflection coefficients are derived from temporal coupled mode theory [48]: $t = -\exp(i\varphi)\frac{1/\tau_e}{i(\omega-\omega_0)+(1/\tau_0+1/\tau_e)}$, $r = \exp(i\varphi)\frac{i(\omega-\omega_0)+1/\tau_0}{i(\omega-\omega_0)+(1/\tau_0+1/\tau_e)}$, where ω_0 is the resonant

Accepted Manuscript
Version of record at: https://doi.org/10.1002/adom.202201193

angular frequency of the localized surface plasmon mode. φ is a plasmonic phase shift. In the hybrid photonic-plasmonic system, the graphene and metal loss impact the Ohmic dissipation rate ($1/\tau_0$). The surface roughness of graphene, metal scattering and ZnSe nonuniformity contributes to the coupling rate to radiation ($1/\tau_e$). Graphene only increases absorption ~2% near the plasmonic resonance frequency while imposes large phase shifts on the complex transmission (t) and reflection (r) spectra, compared to the gold nanorods array. Based on the experimentally fitted parameters, we simulated the spacer thickness dependent absorption spectra (Fig. 2a). The BIC points are highlighted with dashed circles. The metal loss rate to Ohmic dissipation (τ_0 = 0.02 ps) strongly modifies the response in the system (Fig. 2b). By keeping the rest of parameters the same, a reduced Ohmic loss rate brings the system closer to an ideal BIC with zero full-width-half-maximum (FWHM) (blue doted curves in Fig. 2b, τ_0 = 0.2 ps). However, the peak absorption also is reduced to minimal near the BIC (blue curve in Fig. 2b). The metal loss reduces the quality factor near the BIC (black dotted curve in Fig. 2b), but the system can now approach critical coupling near BIC (black curve in Fig. 2b), which results in perfect absorption in the graphene plasmonic layer. We measured the absorption spectra with the spacer thickness D of 1.4 μm (closer to the critical coupling, Fig. 2c) and 2μm (away from the critical coupling, Fig. 2d). Different slot lengths samples are investigated and compared considering fabrication variations. The slot length of 3.4 μm results in the best absorption near critical coupling.

As the conductivity dispersion in graphene plasmon depends on the chemical doping level, the experimentally measured spectra with varying slot lengths (Fig. 3a) are comparable to the three-dimensional FDTD simulation with graphene chemical potential E_F set at 0.26eV (Fig.

Accepted Manuscript
Version of record at: https://doi.org/10.1002/adom.202201193

3b). The solid and dashed curves represent the absorption spectra for identical device designs with and without graphene, respectively. The circles mark the hybrid modes near the fundamental plasmonic mode for BIC, and the triangles mark the second order mode with higher quality factors. Experimentally, the typical chemical potential E_F of transferred graphene layer is around 0.25eV [48-50], with scattering rate ~ 2.3×10^{13} s^{-1} [51]. The graphene's contribution to the total absorption (difference between the solid and dashed curve) is weaker with E_F = 0.12eV (Fig. 3c), as the mode overlap to the graphene layer reduces with the Fermi level modified complex refractive index spectra in graphene (Supplementary Material I). It is noted that near the plasmonic wavelength (photon energy ~ 0.1eV), the interband absorption is prohibited by Pauli blocking, and thus only intraband absorption contributes to the plasmonic mode absorption.

Both modes shift to longer wavelength at increased slot length L, at the fixed lattice constant Λ = 4.0 μm (Supplementary Material II). The maximum peak absorption is achieved at L=3.8 μm and chemical potential of 0.26 eV, which is typical for transferred graphene from copper (Fig. 3b). Significant contrast to control sample without graphene is observed near the fundamental plasmonic mode. A similar trend is observed in the measurements, where the peak absorption in the graphene sample is significantly larger (Fig. 3a). The peak absorption of the hybrid mode increases with the slot length and reaches a peak value near 68% at L = 3.0μm and 3.5μm (solid curves in Fig. 3a). Peak absorption near 53% is shown in the hybrid mode without graphene at L = 3.0μm and decreases with longer L. Compared to the FDTD simulations, the reduced peak absorption in measurement might be attributed to parasitic loss channels such as scattering or polymer residue absorption.

Accepted Manuscript
Version of record at: https://doi.org/10.1002/adom.202201193

The significant absorption enhancement enabled by the graphene monolayer disappears in the hybrid system away from the BIC condition. We examined the hybrid system with half lattice constant Λ = 2.0 μm and the same L/Λ ratio. The resonance frequency of those plasmonic modes nearly doubled, and the photonic and plasmonic modes are decoupled (Fig. 4a). Graphene transferring does not modify the resonance frequencies (dashed and solid curves in Fig. 4a). No clear enhancement in peak absorption is observed for this different lattice constant (Fig. 4b-c). The peak absorptions in a set of devices with Λ = 2.0 μm are consistently lower than the Λ = 4.0 μm devices sets. Both sets of data in Fig. 4 had an optical spacer thickness of 1.4 μm.

4. Conclusions

With practical plasmonic loss rates and radiation loss rates, BIC-enhanced coupling coefficient to the graphene plasmon enables approaching more conveniently the critical coupling condition. Given the chemical potential of transferred CVD graphene, the lack of inter-band transition results in weak absorption in graphene in the far-infrared range. However, the reduction in radiation loss typical of BICs can compensate for this effect and enable critical coupling through photonic engineering. Our numerical simulation predicts over 90% absorption by leveraging the weak intra-band transitions in graphene, and our experiments demonstrate large absorption contrast (50%) by adding a monolayer graphene. These demonstrations set a device framework for free-space graphene switches and imagers operating in mid- and far- infrared ranges.

Supporting Information

Supporting Information is available from the Wiley Online Library or from the author.

Acknowledgments

The authors acknowledge Dr. M. Mironznik for ZnSe thin film preparation. The authors acknowledge discussions with Dr. N. Limberopoulos and Dr. R. Ewing from Air Force Research Laboratory, Sensors Directorate, Wright Patterson AFB. This work is supported by Air Force Office of Scientific Research (AFOSR YIP FA9550-18-1-0300), the Simons Foundation, and the Air Force Office of Scientific Research MURI program with grant No. FA9550-17-1-0002. A. S. is supported by University of Delaware Research Office grants to early-career tenrure track faculty.

Conflict of Interest

The authors declare no conflict of interest.

Received: ((will be filled in by the editorial staff))
Revised: ((will be filled in by the editorial staff))
Published online: ((will be filled in by the editorial staff))

References

[1] T. Low, P. Avouris, *ACS nano* 2014, 8, 1086-1101.

[2] A. N. Grigorenko, M. Polini, K. S. Novoselov, *Nature photonics* 2012, 6, 749.

[3] D. A. Iranzo, S. Nanot, E. J. C. Dias, I. Epstein, C. Peng, D. K. Efetov, M. B. Lundeberg, R. Parret, J. Osmond, J.Y. Hong, J. Kong, *Science* 2018, 360, 291-295.

[4] Q. Guo, F. Guinea, B. Deng, I. Sarpkaya, C. Li, C. Chen, X. Ling, J. Kong, F. Xia, *Advanced Materials* 2017, 29, 1700566.

[5] B. Zeng, Z. Huang, A. Singh, Y. Yao, A. Azad, A. Mohite, A. Taylor, D. Smith, H. Chen, *Light: Science & Applications* 2018, 7, 51.

[6] D. Ansell, I. P. Radko, Z. Han, F. J. Rodriguez, S. I. Bozhevolnyi, A. N. Grigorenko, *Nature communications* 2015, 6 8846.

[7] S. H. Lee, M. Choi, T.T. Kim, S. Lee, M. Liu, X. Yin, H.K. Choi, S.S. Lee, C.G. Choi, S.Y. Choi, X. Zhang, *Nature Materials* 2012, 11, 936–941.

[8] L. Ju, B. Geng, J. Horng, C. Girit, M. Martin, Z. Hao, H.A. Bechtel, X. Liang, A. Zettl, Y.R. Shen, F. Wang, Graphene plasmonics for tunable terahertz metamaterials. *Nature nanotechnology* 2011, 6, 630.

[9] B. Yao, Y. Liu, S.-W. Huang, C. Choi, Z. Xie, J. F. Flores, Y. Wu, C. W. Wang, *Nature Photonics* 2018, 12, 22.

[10] J. Chen, M. Badioli, P. Alonso-González, S. Thongrattanasiri, F. Huth, J. Osmond, M. Spasenović, A. Centeno, A. Pesquera, P. Godignon, Z. A. Elorza, N. Garcia de Camara, F. J. Abajo, R. H. L. Hillenbrand, F. Koppens, *Nature* 2012, 487, 77.

[11] S. Cakmakyapan, P. Lu, A. Navabi, M. Jarrahi, *Light: Science & Applications* 2018, 7, 20.

[12] I.-H. Lee, D. Yoo, P. Avouris, T. Low, S.-H. Oh, *Nature nanotechnology* 2019, 14, 313-9.

[13] F. Liu, E. Cubukcu, *Physical Review B* 2013 88, 115439.

[14] H. Hu, X. Yang, X. Guo, K. Khaliji, S. R. de Biswas, F.J.G. Abajo, T. Low, Z. Sun, Q. Dai, *Nature communications* 2019, 10, 1131.

[15] Y. Zhu, Z. Li, Z. Hao, C. DiMarco, P. Maturavongsadit, Y. Hao, M. Lu, A. Stein, Q. Wang, J. Hone, N. Yu, *Light: Science & Applications* 2018, 7, 1-11.

[16] Z. Li, Y. Zhu, Y. Hao, M. Gao, M. Lu, A. Stein, A. Park, J. Hone, Q. Lin, N. Yu, *ACS Photonics* 2019 6, 501-509.

[17] D. Farmer, P. Avouris, Y. Li, T. Heinz, S. J. Han, *ACS Photonics* 2016, 3, 553-557

[18] Q. Ding, Y. Shi, M. Chen, H. Li, X. Yang, Y. Qu, W. Liang, M. Sun, *Scientific reports* 2016, 6, 32724.

[19] Z.-G. Dai, X.-H. Xiao, W. Wu, Y.-P. Zhang, L. Liao, S.-S. Guo, J.-J. Ying, C.-X. Shan, M.-T. Sun, Z.-Z. Jiang, *Light: Science & Applications* 2015, 4, e342.

[20] V. Semenenko, S. Schuler, A. Centeno, A. Zurutuza, T. Mueller, V. Perebeinos, *ACS Photonics* 2018, 5, 3459-3465.

[21] K. J. Tielrooij, L. Orona, A. Ferrier, M. Badioli, G. Navickaite, S. Coop, S. Nanot, B. Kalinic, T. Cesca, L. Gaudreau, Q. Ma, A. Centeno, A. Pesquera, A. de Zurutuza, H. Riedmatten, P. Goldner, F. J. Garcia de, P. Jarillo-Herrero, F. H. L. Koppens, *Nature Physics* 2015, 11, 281.

[22] Z. Fei, A.S. Rodin, W. Gannett, S. Dai, W. Regan, M. Wagner, M.K. Liu, A.S. McLeod, G. Dominguez, M. Thiemens, A.H.C. Neto, *Nature Nanotechnol*ogy 2013, 8, 821–5.

[23] H. Yan, T. Low, W. Zhu, Y. Wu, M. Freitag, X. Li, F. Guinea, P. Avouris, F. Xia, *Nature Photonics* 2013, 7, 394.

[24] M. B. V. Jang, M. Sherrott, J. Lopez, L. Kim, S. Kim, M. Choi, H. Atwater, *Physical Review B* 2014, 90, 165409.

[25] Z. Fang, Y. Wang, A. Schlather, Z. Liu, P. Ajayan, F. Garcia de Abajo, P. Nordlander, X. Zhu, N. Halas, *Nano Letters* 2013, 14, 299-304.

[26] T. Gu, A. Andryieuski, U. Hao, C. W. Wong, J. C. Hone, A. Lavrinenko, T. Low, T. F. Heinz, *ACS Photonics* 2015, 11, 1552-1558.

[27] G. Ni, A. S. McLeod, Z. Sun, L. Wang, L. Xiong, K. W. Post, S. S. Sunku, B.Y. Jiang, J. Hone, C.R. Dean, M. M. Fogler, D. N. Basov, *Nature* 2018, 557, 530.

[28] Y. Yao, M. Kats, P. Genevet, N. Yu, Y. Song, J. Kong, F. Capasso, *Nano Letters* 2013, 13,

1257-1264.
[29] Y. Jia, H. Zhao, Q. Guo, X. Wang, H. Wang, F. Xia, *ACS Photonics* 2015, 2, 907-12.
[30] O. Salihoglu, S. Balci, C. Kocabas, *Applied Physics Letters* 2012, 100, 213110.
[31] N. Emani, T. Chung, X. Ni, A. Kildishev, Y. Chen, A. Boltasseva, *Nano Letters* 2012, 12, 5202-5206.
[32] F. Yesilkoy, E.R. Arvelo, Y. Jahani, M. Liu, A. Tittl, V. Cevher, Y. Kivshar, H. Altug, *Nature Photonics* 2019, 13, 390-396.

[33] J. R. Piper, S. Fan, *ACS Photonics* 2014, 1, 347.

[34] Y. Liu, A. Chadha, D. Zhao, J. R. Piper, Y. Jia, Y. Shuai, L. Menon, H. Yang, Z. Ma, S. Fan, F. Xia, *Applied Physics Letters* 2014, 105, 181105.

[35] L. Zhu, F. Liu, H. Lin, J. Hu, Z. Yu, X. Wang, F. Fan, *Light: Science & Applications* 2016, 5, e16052.
[36] C.W. Hsu, B. Zhen, A. D. Stone, J. D. Joannopoulos, M. Soljačić, *Nature Reviews Materials* 2016, 1, 1-13.

[37] Z. Yu, X. Xi, J. Ma, H. K. Tsang, C.-L. Zou, X. Sun, *Optica* 2019, 6, 1342-1348.

[38] F. Monticone, A. Alù, *Physical Review Letters* 2014, 112, 213903.

[39] R.E. Jacobsen, A. Krasnok, S. Arslanagic, A.V. Lavrinenko, A. Alù, *ACS Photonics* 2022, 9, 1936-1943.

[40] A. Kodigala, T. Lepetit, Q. Gu, B. Bahari, Y. Fainman, B. Kanté, *Nature* 2017, 541, 196-199.

[41] A. Pavlov, I. Zabkov, V. Klimov, *Optics Express* 2018, 26, 28948-28962.

[42] N. Bernhardt, K. Koshelev, S. J. U. White, K. Wong, C. Meng, J. E. Froch, S. Kim, T. T. Tran, D.-Y. Choi, Y. Kivshar, A. S. Solntsev, *Nano Letters* 2020, 20, 5309-5314.

[43] S. Sun, Y. Ding, H. Li, P. Hu, C.-W. Cheng, Y. Sang, F. Cao, Y. Hu, A. Alù, D. Liu, Z. Wang, *Physical Review B* 103, 045416 (2021).

[44] X. Wang, J. Duan, W. Chen, C. Zhou, T. Liu, S. Xiao, *Physical Review B* 2020, 102, 155432.

[45] S. I. Azzam, V. M. Shalaev, A. Boltasseva, A. V. Kildishev, *Physical Review Letters* 2018, 121, 253901.

[46] Y. Zhou, Z. Guo, X. Zhao, F. Wang, Z. Yu, Y. Chen, Z. Liu, S. Zhang, S. Sun, X. Wu, *Advanced Optical Materials*, p.2200965 (2022).

[47] Marinica, D. C. Borisov, A. G. Shabanov, S. V. Bound states in the continuum in photonics. *Physical Review Letters* 2008, 100, 183902.

[48] L. Malard, M. Pimenta, G. Dresselhaus, M. Dresselhaus, *Physics Reports* 2009 473, 51-87.

[49] W. Gao, J. Shu, K. Reichel, D. V. Nickel, X. He, G. Shi, R. Vajtai, P. M. Ajayan, J. Kono, D. M. Mittleman, Q. Xu, *Nano Letters* 2014, 14, 1242−1248.

[50] H. Hafez, I. Al-Naib, K. Oguri, Y. Sekine, M. M. Dignam, A. Ibrahim, D. G. Cooke, S.

Tanaka, F. Komori, H. Hibino, T. Ozaki, *AIP Advance* 2014, 4, 117118.

[51] J. Buron, F. Pizzocchero, B. Jessen, T. J. Booth, P. F. Nielsen, O. Hansen, M. Hilke, E. Whiteway, P. U. Jepsen, P. Bøggild, D. H. Petersen, *Nano Letters* 2014, 14, 6348−6355.

Accepted Manuscript
Version of record at: https://doi.org/10.1002/adom.202201193

Figures:

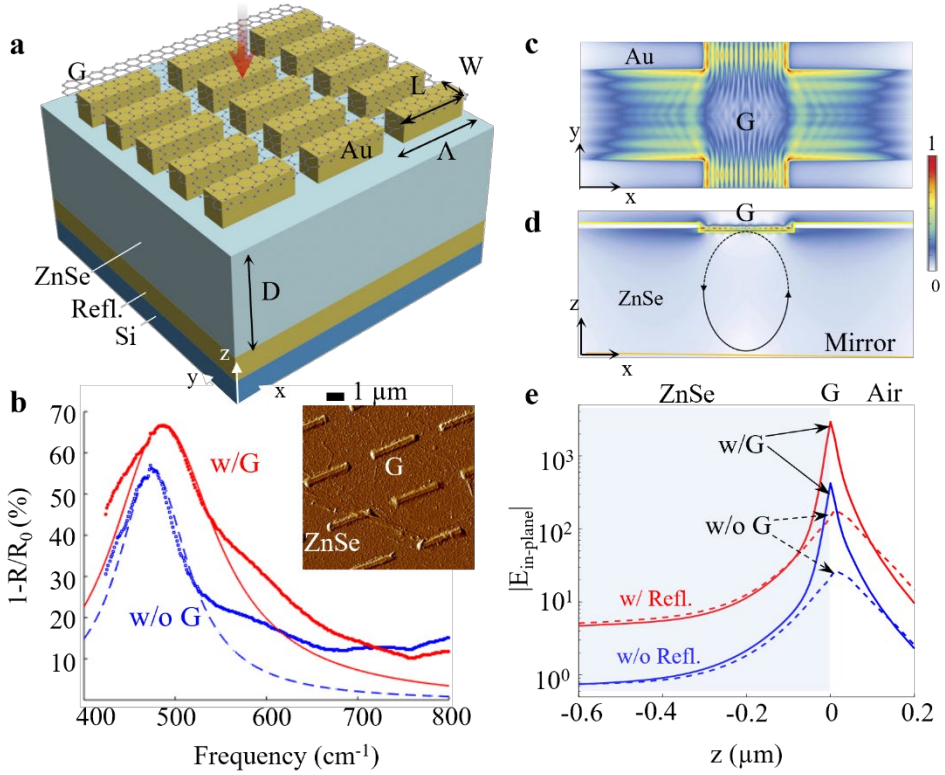

Figure 1. Graphene modified hybrid plasmon-photonic system. a Perspective view of the device. **b** Measured extinction spectra and BIC model fitted spectra (solid and dashed curves) for the given device design (D = 1.4 μm, L = 3 μm, and Λ = 4 μm) with (red dots) and without graphene (blue dots). **c** Optical intensity profile in one primitive cell at plasmonic resonance wavelength in XY plane and **d** XZ plane. **e** Optical intensity distribution along the z-direction across the graphene layer. An order of magnitude higher field intensity is shown for the same design on the graphene layer graphene (solid curves), compared to the control samples without graphene (dashed curves). The effect of the back reflector is shown as the contrast between blue and red curves.

Accepted Manuscript
Version of record at: https://doi.org/10.1002/adom.202201193

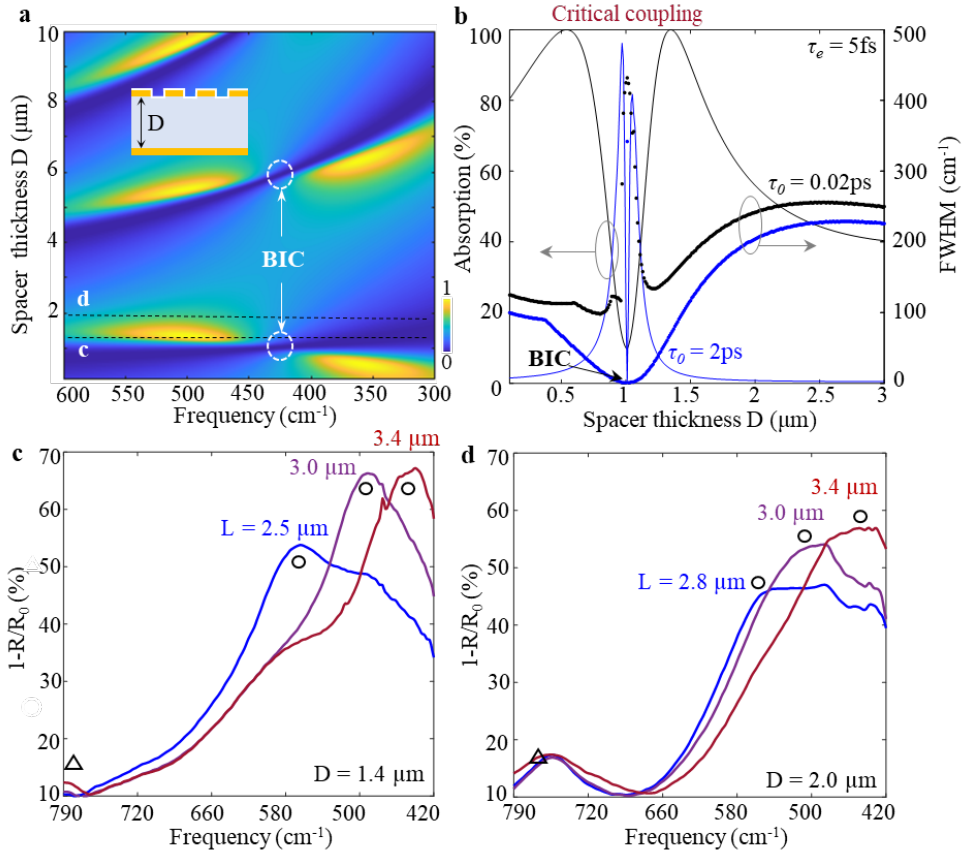

Figure 2. Bound states in the continuum mediated radiation loss and coupling to graphene-metal plasmon polariton. a Simulated absorption spectra versus spacer thickness D based on equation (1). The plasmonic mode frequency is 430 cm^{-1}. The Ohmic loss lifetime $\tau_0 = 0.02$ ps and the radiation coupling lifetime $\tau_e = 5$ fs are obtained by fitting the experimental results. The dashed circles mark the BIC states in the lossy system. **b** Photonic mode dependent peak absorption and full width half maximum width (FWHM). With the same τ_e, and the metal loss lifetime is set to be 2ps (more ideal case, blue curves) and 0.02ps (experimental value, black curve). **c** Measured extinction spectra for D = 1.4 μm and **d** D = 2.0 μm. The lattice constant $\Lambda = 4.0$ μm. The results for the rod length L=2.5, 3.0 and 3.4 μm are plotted in blue, purple and red respectively in **c** and **d**.

Accepted Manuscript
Version of record at: https://doi.org/10.1002/adom.202201193

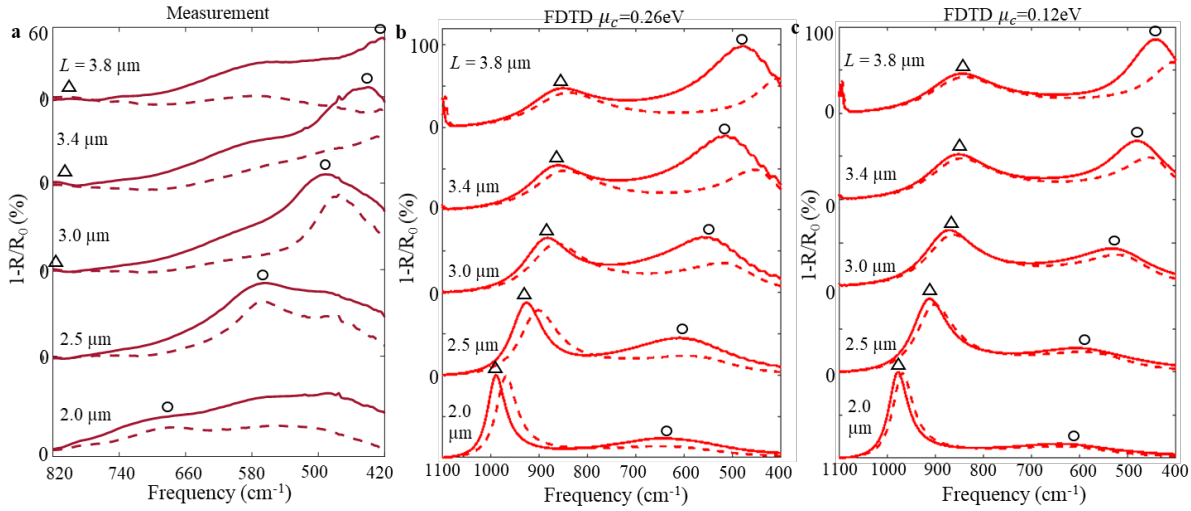

Figure 3. Graphene Fermi-level dependent absorption contrast. a Measured extinction spectrum with (solid curves) and without (dashed lines) graphene. **b** Full field numerical simulation of the correspondent extinction spectra with the Fermi level of graphene set at 0.26eV and **c** 0.12eV. The empty circles and triangles mark the first and second order plasmonic mode. The spacer thickness is 1.4 μm. Lattice constant is 4μm. The rod length increases from 2 μm to 3.8 μm.

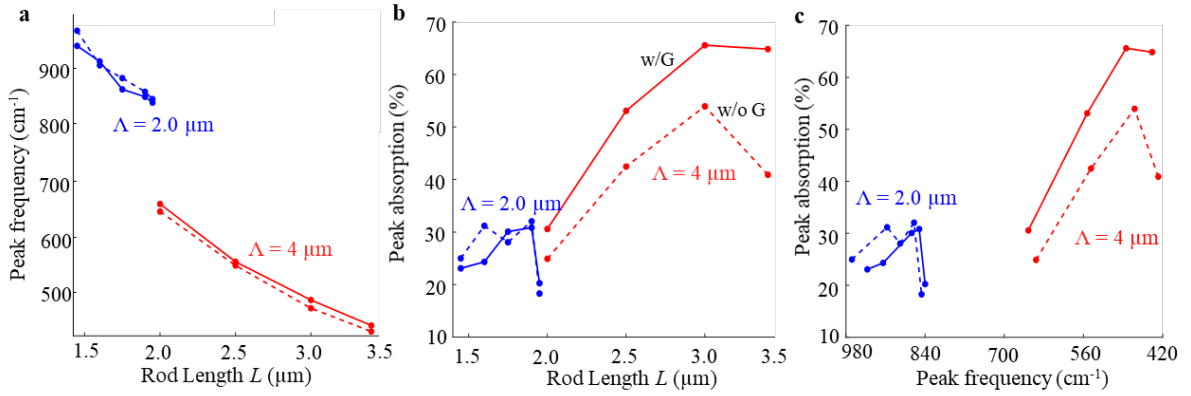

Figure 4. Lattice constant dependent resonance frequencies and peak absorption of the hybrid mode with (solid lines) and without graphene (dashed lines). **a** Critical wavenumber and **b** Extinction ratio as a function of rod length L for Λ = 2.0 μm (blue) and Λ = 4.0 μm (red). as a function of rod length. The smaller periodicity reaches a maximum extinction ratio at L = 1.9 μm and the larger periodicity reaches a maximum at L = 3.0 μm. **c** Extinction spectra as a function of critical wavenumber.